AGU PUBLICATIONS

JGR

Journal of Geophysical Research: Oceans

RESEARCH ARTICLE

10.1002/2016JC012464

Circulation, hydrography, and transport over the summit of Axial Seamount, a deep volcano in the Northeast Pacific

G. Xu[1] and J. W. Lavelle[2]

[1]Geology and Geophysics, Woods Hole Oceanographic Institution, Woods Hole, Massachusetts, USA, [2]National Oceanic and Atmospheric Administration, Pacific Marine Environmental Laboratory, Seattle, Washington, USA

Key Points:
- Anticyclonic toroidal mean and barotropic/internal tidal currents dominate motion at the summit of Axial
- Time-averaged temperature and salinity show lateral gradients within the caldera while their anomalies dome above the seamount
- Passive tracers originating inside the caldera are trapped to Axial before eventually bleeding off into the distal ocean

Supporting Information:
- Supporting Information S1
- Figure S1
- Data Set S1
- Data Set S2
- Movie S1
- Movie S2

Correspondence to:
G. Xu,
gxu@whoi.edu

Citation:
Xu, G. and J. W. Lavelle (2017), Circulation, hydrography, and transport over the summit of Axial Seamount, a deep volcano in the Northeast Pacific, *J. Geophys. Res. Oceans*, *122*, 5404–5422, doi:10.1002/2016JC012464.

Received 12 OCT 2016
Accepted 19 MAY 2017
Accepted article online 24 MAY 2017
Published online 7 JUL 2017

Abstract A numerical model of ocean flow, hydrography, and transport is used to extrapolate observations of currents and hydrography and infer patterns of material flux in the deep ocean around Axial Seamount, a destination node of NSF's Ocean Observatories Initiative's Cabled Array. Using an inverse method, the model is made to approximate measured deep ocean flow around this site during a 35 day time period in the year 2002. The model is then used to extract month-long mean patterns and examine smaller-scale spatial and temporal variability around Axial. Like prior observations, model month-long mean currents flow anticyclonically around the seamount's summit in toroidal form with maximum speeds at 1500 m depth of 10–11 cm/s. As a time mean, the temperature (salinity) anomaly distribution takes the form of a cold (briny) dome above the summit. Passive tracer material continually released at the location of the ASHES vent field exits the caldera primarily through its southern open end before filling the caldera. Once outside the caldera, the tracer circles the summit in clockwise fashion, fractionally reentering the caldera over lower walls at its north end, while gradually bleeding southwestward during the modeled time period into the ambient ocean. A second tracer release experiment using a source of only 2 day duration inside and near the CASM vent field at the northern end of the caldera suggests a residence time of the fluid at that locale of 8–9 days.

1. Introduction

Axial Seamount is an episodically active underwater volcano that lies more than 1420 m below the sea surface and some 450 km off the Oregon Coast on the Juan de Fuca Ridge (JdFR) near 130°01′W and 45°57′N (Figure 1a). The seamount, located near the junction of the Axial and CoAxial segments of the ridge is thought to be the result of a magmatic hot spot located under the spreading ridge [*Carbotte et al*., 2008]. Axial is the youngest of volcanoes in the Cobb-Eikelberg seamount chain, a string of volcanoes that trend off to the WNW. The nearest volcano in the chain to the west is Brown Bear, a taller and areally larger seamount located at a distance of no more than 30 km (Figure 1b). At the summit of Axial, the horse-shoe-shaped topographic highs define the volcano's caldera (Figure 2). The caldera wall, nominally ∼100 m above the caldera floor, is higher on the west than east. At the northern end of the caldera a topographic saddle can be found.

Physical, chemical, biological, geological, and geophysical conditions at Axial have been monitored extensively in the last three decades [e.g., *Chadwick et al*., 2010]. Most pertinent to the present study are the physical oceanographic observations. Current meter observations along much of the extent of the Juan de Fuca Ridge highlight an anticyclonic mean-current shear across and within ∼10 km of the ridge [e.g., *Cannon and Pashinski*, 1997]. Away from the ridge at greater distances but at near-ridge depths (1800–2200 m), year-long measurements, primarily sampled to the west, shows mean currents of only 0.02–1.7 cm/s with highly variable direction [*Cannon et al*., 1993]. On the other hand, *Cannon et al*. [1995] report year-long (1992–1993) mean flow from four mooring with speeds of 2–3 cm/s crossing the JdFR toward the E and SE at a site ∼50 km south of Axial. Year-long mean current speed and direction at ridge depth in this region are thus far from steady. Variability of magnitude is also true for the subinertial flow having an unusual spectral peak at a period of approximately 4 days (the weather band (WB)) [*Thomson et al*., 1990; *Cannon and Thomson*, 1996], a spectral line commonly observed along the ridge, though more prominent in winter months. *Cannon and Pashinski* [1990] also reported moderate, vertically sheared year-long deep mean flow

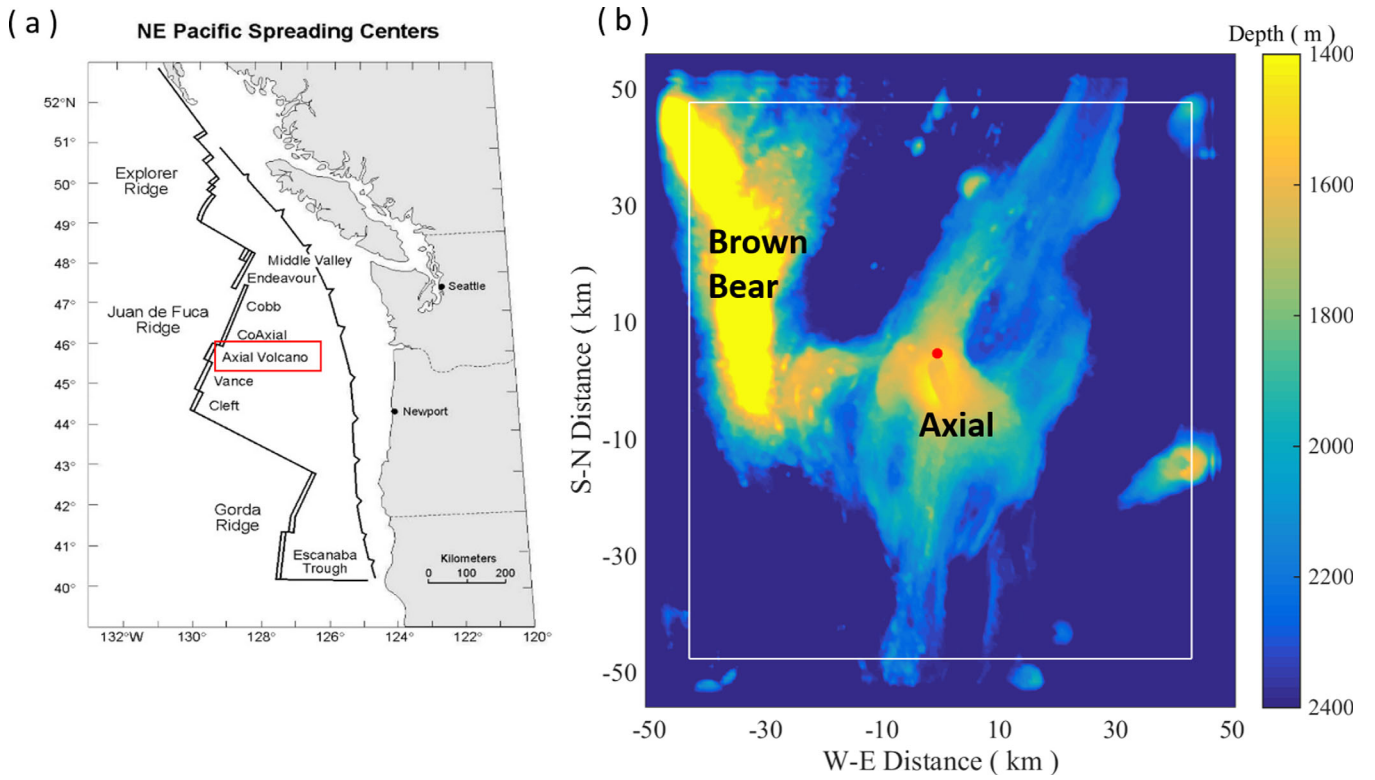

Figure 1. (a) Location of Axial Seamount on the Juan de Fuca Ridge. (b) Bathymetry within the model domain. The white line marks the inner edge of the "pretty good sponge" zone used to absorb the waves generated in the model interior. The red dot indicates the location of a mooring deployed at Axial in 2001–2002.

at a site between Axial and Brown Bear and topographically steered flow from a month-long mooring at a site within the caldera and near the west wall. A later, more extensive set of current meter data at Axial showed time-mean clockwise flow circulating around Axial with maximum speed of 6.6 cm/s at 1575 m depth [*Lavelle et al*., 2003]. That analysis showed the topographic trapping of subinertial flows, with diurnal and weather band (WB) motions amplified near the seamount. Similar topographic trapping of subinertial flows has been studied extensively, but in particular in this part of the ocean along deep ocean ridges by, for example, *Allen and Thomson* [1993] and *Berdeal et al*. [2006].

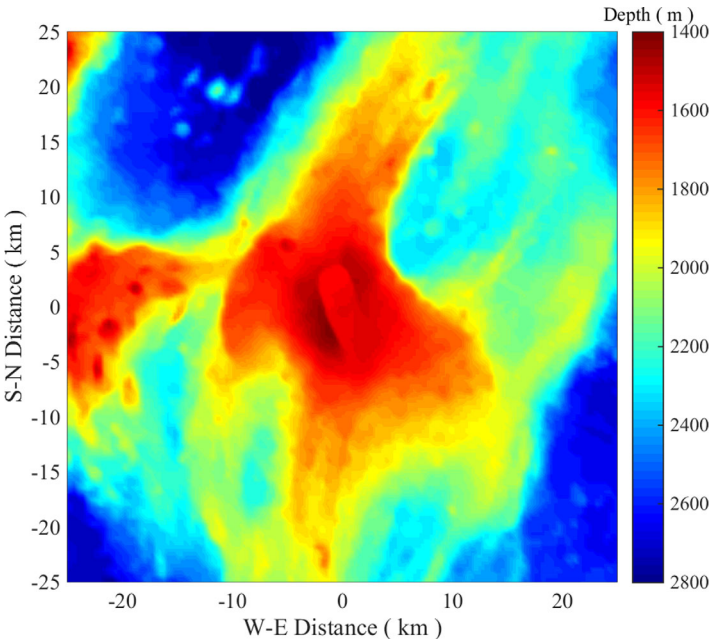

Figure 2. Close-up of the topography of Axial. The co-ordinate origin is located at 45.958°N, 130.010°W.

Axial is one of the most active volcanic sites in the Northeast Pacific, based on ocean acoustic observations dating to the early 1990s [*Dziak et al*., 2011]. Volcanic eruptions are known to have occurred at Axial in January 1998 [*Dziak and Fox*, 1999; *Embley et al*., 1999; *Resing et al*., 1999], April 2011 [*Chadwick*

et al., 2012], and most recently in April 2015 [*Kelly et al*., 2015; *Delaney*, 2015]. Superimposed on this eruptive activity are continuous hydrothermal discharges at numerous sites within Axial's caldera and nearby. Within the caldera there are three main hydrothermal vent fields [*Kelly et al*., 2014]: CASM (Canadian American Seamount Expedition) at the northern end of the caldera, ASHES (Axial Seamount Hydrothermal Emissions Study) near the southwestern rim of the caldera, and International District in the southern rift zone. ASHES and CASM are sites we chose as source locations for tracer dispersion experiments that will be described later.

Currents within the caldera [e.g., *Tivey et al*., 2002] and beyond are of particular interest in that they transport and disperse chemical [e.g., *Resing et al*., 1999] and microbiological materials [*Huber et al*., 2006; *Opatkiewicz et al*., 2009] emanating from hydrothermal vents. Chemical species [e.g., *Lupton et al*., 1999] and particulates [e.g., *Feely et al*., 1992] at Axial, in return, aid in the interpretation of transport patterns. Of equal interest are the transport pathways and the residence time of fluid in and around the seamount in relationship to the dispersion of macrofaunal larvae. As sources of energy, vent sites are habitats for many benthic animals [*Limen et al*., 2007; *Kelly and Metaxas*, 2008]. The dispersion of larvae of those macrofauna bears directly on the issue of community succession at those vent sites [*Marcus et al*., 2009]. Dispersion patterns of biological species at the seamount, along the connected Juan de Fuca Ridge, or into the less hospitable off-axis ocean will also ultimately contribute to the understanding of genetic connectivity of biological species and habitats within the deep ocean [e.g., *Shanks*, 2010].

Axial's high level of magmatic activity and hydrothermal fluid flux from the subseafloor and the fact that the seamount has been monitored since the 1980s made Axial a successful candidate for becoming a primary node on NSF's underwater cable experimental program known as OOI (Ocean Observatories Initiative) [*Cowles et al*., 2010; *Kelly et al*., 2014]. The observatory at Axial—the Cabled Array—was fully installed in 2014. The streaming of real-time multidisciplinary data recorded by observatory instruments came online in 2015. Those data can be readily accessed from laboratories, schools, and homes around world through the World Wide Web via OOI's data portal (https://ooinet.oceanobservatories.org/).

To provide a physical oceanographic framework for interpreting the vast amount of data previously acquired and to be acquired by the Cabled Array, a numerical hydrodynamical model was configured for conditions at Axial to explore patterns of motion, hydrography, and transport there. This paper is a descriptive account of patterns from these regional-scale numerical experiments in the context of field observations at Axial found in earlier works [*Cannon and Pashinski*, 1990; *Lavelle et al*., 2003]. The model and the earlier measurements together allow relevant oceanographic fields (3-D flow velocities, temperature, salinity, etc.) to be extrapolated in time and space with sufficient site density that fluxes (transports) and their patterns and time histories can be quantitatively evaluated.

2. Method

2.1. Model Design and Configuration

The regional numerical model used to investigate motion, hydrography, and transport at Axial is similar to the model used to investigate flow over the East Pacific Rise at 9°N–10°N [*Lavelle et al*., 2010]. The model is a 3-D hydrostatic, free-surface, f-plane, baroclinic hydrodynamic construct for a domain that is open to flow on all four sides. The model uses measured hydrography profiles as initial conditions and as constraints on temperature and salinity around the domain boundaries. Current meter data at a measurement site above Axial at 950 m depth (red dot in Figure 1b) is used to develop the time dependent forcing time series, in a manner described below.

The model domain is a nearly square region ~100 km on each side and centered in Axial's caldera (Figure 1b). Gridded bathymetry data were acquired from the Global Multi-Resolution Topography (GMRT) Synthesis of Marine Geoscience Data System (MGDS) (http://www.marine-geo.org/tools/GMRTMapTool) at 84 m horizontal resolution. For our model use, the bathymetry data were first regridded to 700 m horizontal resolution using a spatial median filter. The median filter provided a median value over the 700 m by 700 m area centered at each coarser grid-cell center. The value 700 m was approximately the smallest wave length resolvable with the grid size to be used.

The smoothed, windowed bathymetric data were interpolated onto a computational grid having 256 × 256 × 128 cells stretched in each of the *x-y-z* directions. The finest resolution (dx = 262 m, dy = 290 m, dz = 13 m) occurred near the center of the caldera at 1400 m depth. That allowed the caldera to be resolved with 24 computational cells in the N-S and 10 cells in the E-W directions. Grid spacing increased parabolically reaching maxima near domain boundaries of dx = 651 m, dy = 721 m, dz =43 m. Model base depth was set to 2800 m given that 97% of depths in the model domain were shallower. Model time step was 45 s.

The model used is a hydrostatic one. The criterion that indicates that hydrostatic dynamics is suitable for this model application comes from the work of *Marshall et al*. [1997]. In the process of developing the MITgcm, they looked at a progression of models from hydrostatic, to quasi-hydrostatic, to nonhydrostatic, and outlined a derivation of a nondimensional number that can be used to judge whether hydrostatic or nonhydrostatic dynamics are appropriate. When the square of ratio of the lateral advective time scale L/U (U is a characteristic velocity over length scale L) to the buoyancy period, $1/N$, is small, then nonhydrostatic dynamics are required. On the other hand, if $(U/(LN))^2 \ll 1$, nonhydrostatic effects need not be considered. Using an average N^2 of 2.53 × 10^{-6} (rad/s)^2 below 1200 m in our modeled region, a characteristic U equal to 0.1 m/s, and a conservative minimum characteristic L of 260 m, the value of their criterion $(U/(LN))^2 = 0.059$, which is $\ll 1$. Thus, a hydrostatic model for Axial is appropriate at the spatial resolution we employ.

This model uses surface forcing rather that boundary forcing to drive the flow. Forcing takes the form of lateral gradients of a planer surface elevation (η_B) controlling the barotropic flow in the region, the normal vector to which reorients in *x-y-z* space each model time step. Surface gradients $\partial(\eta_B)/\partial x$ and $\partial(\eta_B)/\partial$y are derived by assuming that, in the far-field, an adequate representation of the dynamic balance of the barotropic flow there is $\partial u/\partial t = -g\ \partial(\eta_B)/\partial x + fv$ and $\partial v/\partial t = -g\ \partial(\eta_B)/\partial y\text{-}fu$, where u and v are the eastward and northward components of the barotropic currents at a single point, f is the Coriolis parameter, and g is the gravitational constant. Baroclinic currents and an associated surface elevation (η) are generated within the model domain as a result of the barotropic forcing over this stratified region of irregular topography. Outgoing baroclinic motion is sponged back to barotropic values, i.e., baroclinic waves are smothered at the outer domain edges, using the pretty-good-sponge of *Lavelle and Thacker* [2008]. Zero velocity, free surface, and property gradients are imposed on domain boundaries.

The inferred forcing time series is constructed from a single point current meter. This is not ideal, but several comparisons of deep currents from large scale models with observations, suggested to us that, even if year 2002 large-scale model results were available, matching current observations at Axial using them would be difficult. The inverse procedure, described in the following paragraph, yields a forcing series that fairly well reproduces a number of observations in the vicinity of the seamount. Model forcing derived in this way also has the advantage of using a fuller frequency spectrum of forcing motions. "Full-spectrum" forcing allows a broader range of frequencies to dictates magnitudes of mixing via the turbulence submodel. Because of the complexity of the topography in the model region, however, the fidelity of the model description undoubtedly diminishes as radial distance from the seamount grows. For that reason, this paper is focused on flow in the caldera and near the seamount.

The barotropic surface forcing time series is derived iteratively by inversion. The inverse procedure considers the model to be a Green's function linking, via a convolution in the time domain, input currents, as a surrogate for a barotropic forcing time series, to barotropic/baroclinic output currents. At tidal and higher frequencies the model is primarily a linear one. The Convolution Theorem allows the time-domain convolution to be reexpressed in the frequency domain as an algebraic relationship connecting input and output current spectra via the model spectrum G in the form $u\_\text{out}(\omega) = G\_\text{model}(\omega) \times u\_\text{in}(\omega)$, where all three factors are complex numbers, u is a vector current, and ω represents each spectral frequency. Using the observed single point current time series at diminished amplitude as a first guess (using 1 to label that), the $u\_\text{in}_1(\omega)$ and $u\_\text{out}_1(\omega)$ allow $G\_\text{model}(\omega)$ at each ω to be defined. Then a second or later iteration input $u\_\text{in}_2(t)$ can be derived by requiring that the target $u\_\text{out}_2(t)$ should be the observed time series ($u\_\text{meas}(t)$), i.e., $u\_\text{meas}(\omega) = G\_\text{model}(\omega) \times u\_\text{in}_2(\omega)$. Since $G\_\text{model}(\omega)$ is known from the first iteration, $u\_\text{in}_2(\omega)$ and thus $u\_\text{in}_2(t)$ are then easily derived from this last equation, though improbably small values of $u\_\text{in}_1(\omega)$ as denominators for some frequencies in the inversion cannot be allowed to dominate the estimate of $u\_\text{in}_2(\omega)$. The method's utility in finding a suitable input current, $u\_\text{in}_2(t)$, which is then recast as a barotropic

Table 1. Harmonic Analysis Results for Major Tidal Constituents in the Measured and Model Currents Shown in Figure 5[a]

	Measurement				Model			
	Major Axis (cm/s)	Minor Axis (cm/s)	Inclination Angle (degree)	Phase Angle (degree)	Major Axis (cm/s)	Minor Axis (cm/s)	Inclination Angle (degree)	Phase Angle (degree)
M_2	5.35±0.51	2.03±0.51	111.80±6.85	206.71±6.87	5.68±0.62	2.75±0.62	100.74±9.18	194.30±9.12
S_2	1.70±0.51	0.40±0.51	90.28±18.60	230.96±18.69	2.03±0.62	0.60±0.62	103.29±20.13	235.36±19.97
K_1	1.50±0.13	0.50±0.09	107.56±4.27	230.37±5.45	1.45±0.15	0.55±0.10	109.59±5.10	230.05±7.07
O_1	0.87±0.13	0.23±0.09	102.96±6.52	195.29±8.76	0.95±0.16	0.24±0.09	99.17±6.09	188.85±9.87

[a]The harmonic analysis was conducted using T-Tide developed by *Pawlowicz et al*. [2002].

forcing time series, is demonstrated in the correspondence of observed and modeled currents as in Figure 5 and Table 1. A more detailed description of the inverse method can be found [*McGillicuddy et al*., 2010; *Lavelle et al*., 2010].

The profiles of potential temperature (θ) and salinity (S) used to initialize the hydrography fields come from the 2009 World Ocean Atlas annual-averaged profiles interpolated laterally to the coordinates 130.4°W, 45.6°N and then vertically to model grid depths (Figure 3). Resulting profiles were then smoothed with a 5-point Hanning window. A single θ value at 43 m was reset to 10.5°C to allow a larger model time step. No hydrography profiles were taken near Axial in 2002, as best we are aware, but θ and S profiles at Axial from a previous year are very similar to those in Figure 3.

The model equation set is described in detail in *Lavelle* [2006]. A few minor differences with that study include setting minimum vertical and horizontal mixing coefficients to 1 cm^2/s and 1 m^2/s and giving the ratio of the Richardson number (Ri) to Prandtl number (Pr), i.e., the flux Richardson number ($Rf = Ri/Pr$), a fixed value of 0.5. That ratio appears in the factor $(1 - Ri/Pr)^{1/2}$ in the vertical turbulent mixing parametrization of this model. If Rf is <0, the water column is unstable and if $Rf >= 1$, vertical turbulent mixing is extinguished. Because no consensus seems to exist on the dependence of Ri on Pr nor on a value of Pr (here 3.0), we justify the Rf value assigned by the reasonableness of resulting values for vertical mixing. Vertical mixing coefficients remained in an acceptable range of 1 cm^2/s (approximate abyssal background) away from topography to 6 cm^2/s near topography.

2.2. Forcing Currents

Currents used to derive model forcing were measured hourly north of the caldera (red dot in Figure 1b) at 950 m depth using an Aanderaa RCM-7 rotor and vane current meter. A 45 day time interval (21 June to 5 August 2002) of SW flow with a mean speed of nearly 2 cm/s was chosen as the simulation interval to focus on. The rotary periodograms of currents at depths 950 and 1550 m on that mooring over that time period were subsequently calculated (Figure 4). The periodogram of measured currents at 950 m depth (Figure 4a) shows significant peaks at semidiurnal (M_2, S_2), diurnal (K_1), and near-inertial frequencies, with all three oscillations polarized counterclockwise. At greater depth (1550 m), 20 m above the seafloor, the periodogram (Figure 4b) shows significant peaks at diurnal (K_1, O_1), semidiurnal (M_2), and weather band (WB) 3–6 day oscillations. The diurnal and WB oscillations are amplified while semi-diurnal and inertial motions are attenuated in comparison to periodogram at

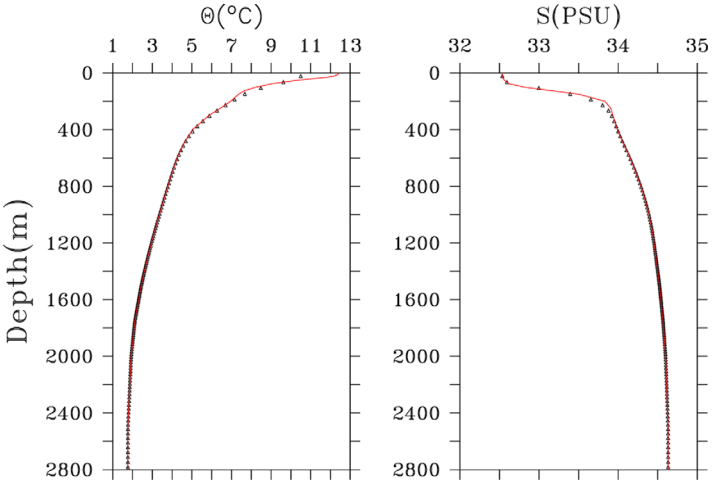

Figure 3. Background potential temperature (θ) and salinity (S) profiles used as the model's initial and boundary conditions (triangles) have been over-plotted in red with the annual-averaged World Ocean Atlas profile data.

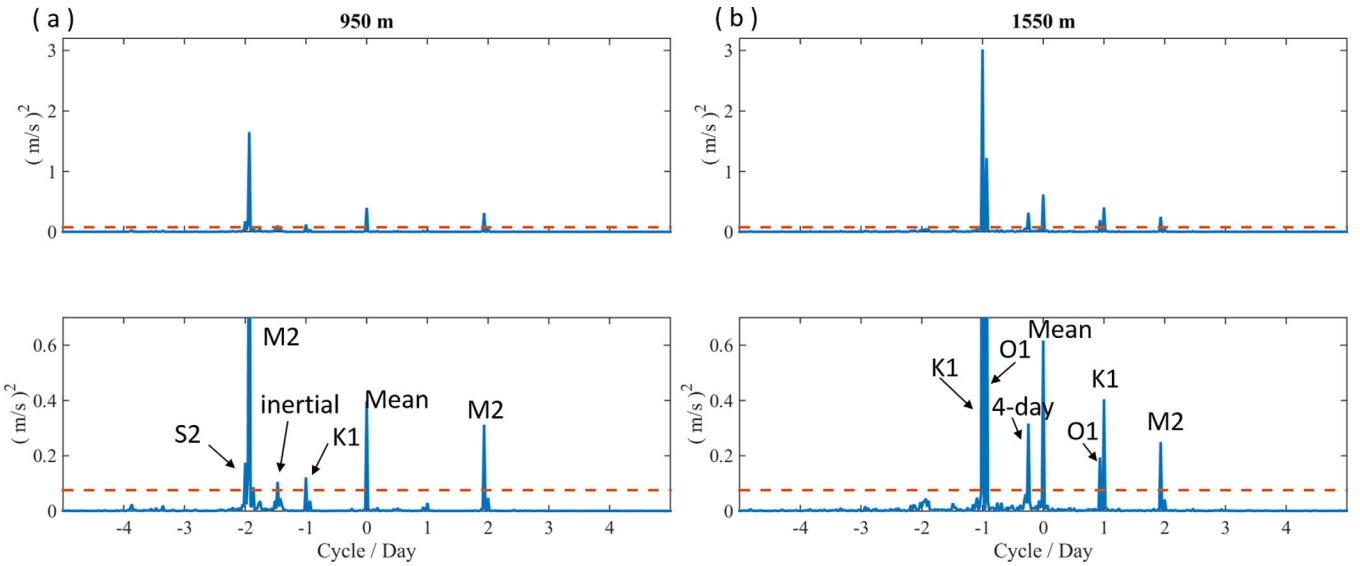

Figure 4. Periodograms of currents measured from 21 June to 5 August 2002 just north of the caldera (red dot in Figure 1b) at (a) 950 m and (b) 1550 m depth. The horizontal dashed lines mark the 95% confidence level. Negative frequencies correspond to clockwise components while positive frequencies correspond to counterclockwise components. The top plots show full ranges of the amplitudes while the bottom plots are clipped at 0.7 $(m/s)^2$ to make the lower peaks stand out more clearly. The frequency components with peaks above the significance level are labeled.

950 m. Amplification of diurnal and WB oscillations, both subinertial, near the seafloor are consistent with observations at Axial [*Cannon and Pashinski*, 1990; *Lavelle et al*., 2003] and much previous theoretical work [e.g., *Chapman*, 1989; *Brink*, 1990; *Allen and Thomson*, 1993].

Model forcing was derived from the measured currents at 950 m depth using the inverse method described in the previous section using two sequential model runs. This inverse-derived model-forcing time series was subsequently altered by using a linear ramp to bring forcing from zero to full value over an initial four simulation days. This allowed dissipative terms to become large-enough that startup instability was controlled. A

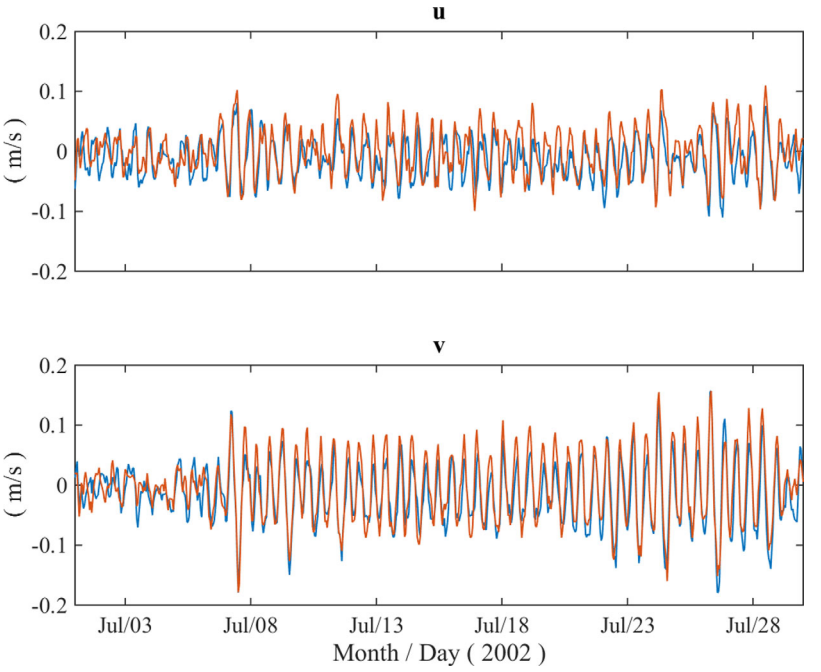

Figure 5. Comparison between the eastward (u) and northward (v) components of the measured (blue) and model (red) currents from 1 July to 30 July 2002 at 950 m depth at a location just north of the caldera (red dot in Figure 1b).

subsequent period of 6 days before model result sampling began permitted model currents to achieve quasi-equilibrium.

Comparisons of measured and simulated N-S and E-W current components at 950 m depth show that the iterative force-finding procedure causes the phases of model and measured currents to be matched (Figure 5). Correlation coefficients for modeled and measured zonal (u) and meridional (v) current time series at the 950 m site are 0.73 and 0.89, respectively. Harmonic analysis results (Table 1) for the major tidal constituents (M_2, S_2, K_1, O_1) show even better correspondence with all values within the range of estimation uncertainties. The model mean current is 0.5 cm/s in the southward direction.

3. Results and Discussion

3.1. Mean Horizontal Circulation

Model output averaged over a 29.5 day period following the initial 10 day spin-up shows mean circulation at Axial is anticyclonic around the seamount's summit (Figure 6). Transects across the model summit indicate that the mean flow takes the form of a torus trapped to the summit flanks. Largest flows in the toroid (~10–11 cm/s) at 1500 m depth are found in the south west sector, where the walls of the caldera are the highest. No current meter data are available at the location, but *Lavelle et al*. [2003] reported a year-long mean flow westward of 6.6 cm/s for a site at 1575 m depth due south of the caldera. The model flow away from the Axial toroid is considerably weaker, a result that is consistent with the field observations reported in *Lavelle et al*. [2003].

To investigate how much the presence of the taller, areally bigger Brown Bear Seamount 30 km west of Axial could influence deep ocean conditions and flows near Axial, we conducted a separate simulation with seafloor topography to the west of Axial clipped at 2000 m depth while keeping all other model inputs and configurations the same. The results (e.g., Figure 6b) suggest mean circulation (e.g., clockwise toroidal flow) remain basically unchanged within the immediate vicinity and to the east of Axial. In addition, the instantaneous model currents from the two experiments at the mooring marked in Figure 1b at 950 m depth have correlation coefficients of 0.84 and 0.94 for u and v components. Discernible differences start to appear in regions >10 km to the west of Axial. This result suggests the presence of Brown Bear has limited influences on flows in the immediate vicinity of Axial, which is the focus area of this study.

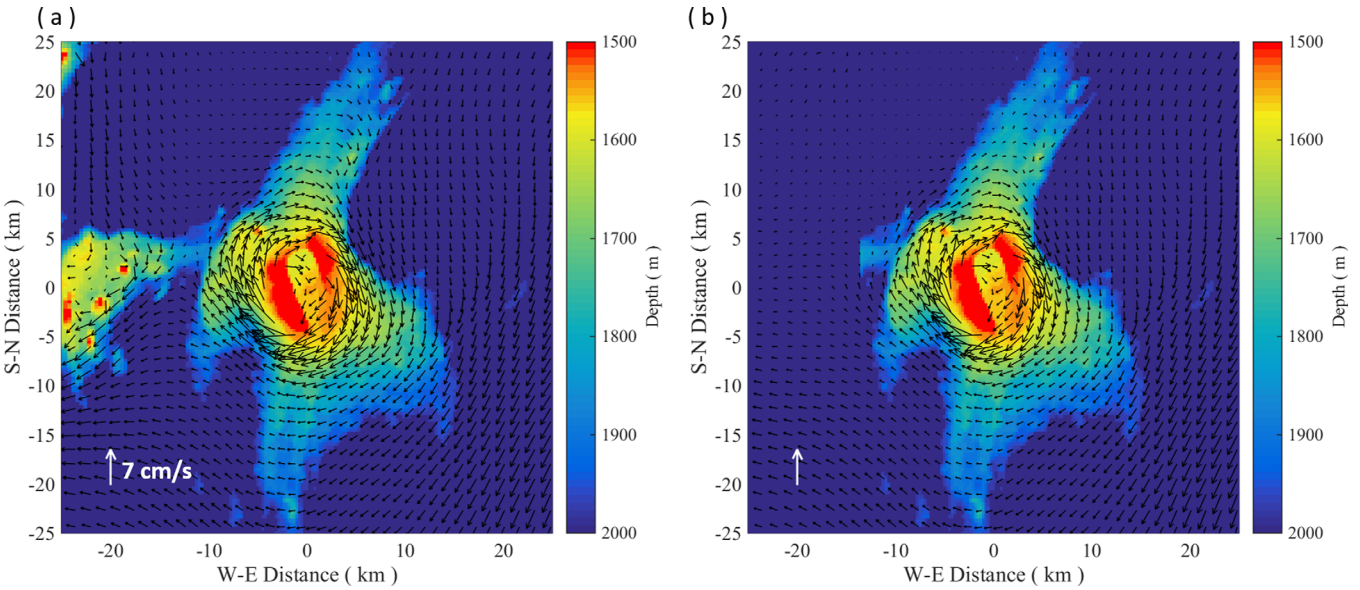

Figure 6. (a) Model velocity vectors at 1500 m depth averaged over a 29.5 day period beginning 1 July 2002. Largest vectors are on the order of 10 cm /s. The coordinate center is the same as in Figure 2. (b) Same as (a) except they result from the simulation with seafloor topography to the west of Axial clipped at 2000 m depth to remove Brown Bear from the model bathymetry.

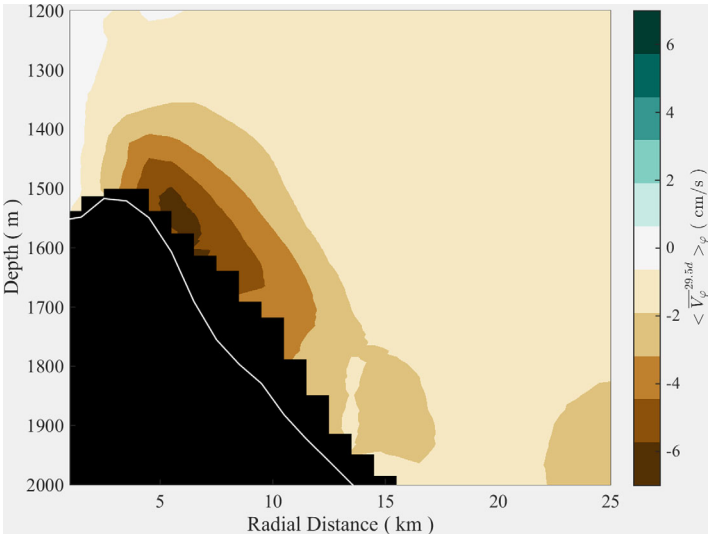

Figure 7. Azimuthally averaged, time-averaged azimuthal velocities. Negative values correspond to anticyclonic flows. The coordinate origin is the same as in Figure 2. The curve in white represents the azimuthal mean bathymetry.

The vertical structure of the toroidal mean flow is revealed (Figure 7) most clearly by the azimuthally averaged azimuthal velocity of the 29.5 day mean flow ($\langle \bar{V}_{\varphi}^{\,29.5d} \rangle_{\varphi}$) with respect to the coordinate origin cited in Figure 2. This calculation isolates azimuthal mode-zero motions. At each depth, azimuthal velocities at grid points that fell into 1 km wide concentric annular bins were averaged for bins extending radially to a distance of 25 km. When more than 50% of the grid points in any annular bin were located below the seafloor, the average was designated to be indeterminate. The result (Figure 7) shows the core of the toroid (speed $>$ 6 cm/s) is located 5–7 km radially from the origin and in the 1500 to 1600 m depth interval.

Previous studies suggest residual circulations around abrupt topographic features can form through a variety of different mechanisms, which include: (1) Taylor cap formation in the presence of incident mean flows [*Hogg*, 1973; *Freeland*, 1994; *Codiga and Eriksen*, 1997], (2) rectification of oscillatory flows [*Zimmerman*, 1980], (3) eddy-topography interaction [*Holloway*, 1987]. *Lavelle et al*. [2003], based on analysis of long-term current measurements, suggested both Taylor cap formation and rectification of oscillatory currents can contribute to the clockwise residual circulation at Axial. The study of *Pingree and Maddock* [1985] suggested the rectification of impinging clockwise circular oscillatory currents preferentially generates a clockwise residual flow. The fact that the tidal and inertial oscillations are both circular clockwise in the forcing currents (Figure 4) supports the idea that rectification of oscillatory flows contributes to the clockwise vortex around Axial. On the other hand, anticyclonic residual circulation can form as a Taylor cap, which is a result of conservation of potential vorticity when steady, stratified flows pass over a seamount or ridge. This second mechanism is exemplified in the modeling work of *Chapman and Haidvogel* [1992]. The third mechanism, eddy-topography interaction, is unlikely to be the cause of the residual circulation because the background forcing used in our simulation is spatially uniform and hence free of eddy structures.

To examine which of the first two mechanisms might be more important at Axial, we conducted a separate simulation run with background forcing derived from a steady SW flow of 2 cm/s. The resulting mean flow field exhibits no apparent toroidal circulation around Axial (see Figure S1 in supporting information). This suggests the rectification of oscillatory flows, as opposed to Taylor cap formation, is most likely the dominant causal mechanism for the clockwise circulation around Axial.

3.2. Vertical Circulation

Figure 8 shows the mean and maximum vertical flows near Axial at 1500 m depth. Those results suggest strong vertical flows occur where the topographic gradients are steep (e.g., the rim of the caldera). Near the summit, vertical flows are generally upward within the caldera and downward along its outer rim (Figure 8a). In addition, the magnitudes of maximum vertical flows reach 3 cm/s along the inner edge of the caldera wall (Figure 8b). Vertical flows this strong may be susceptible to field measurement.

Areal patterns of flow through three horizontal surfaces and within three layers defined by those surfaces give further understanding of flux within the caldera. Layers 1, 2, and 3 have horizontal bounding surfaces, respectively, at the caldera floor and 1536 m depth, at 1536 m and 1482 m (the vertical cell interface level closest to the crest of the lower, eastern caldera wall) depths, and at 1482–1420 m (the vertical cell interface

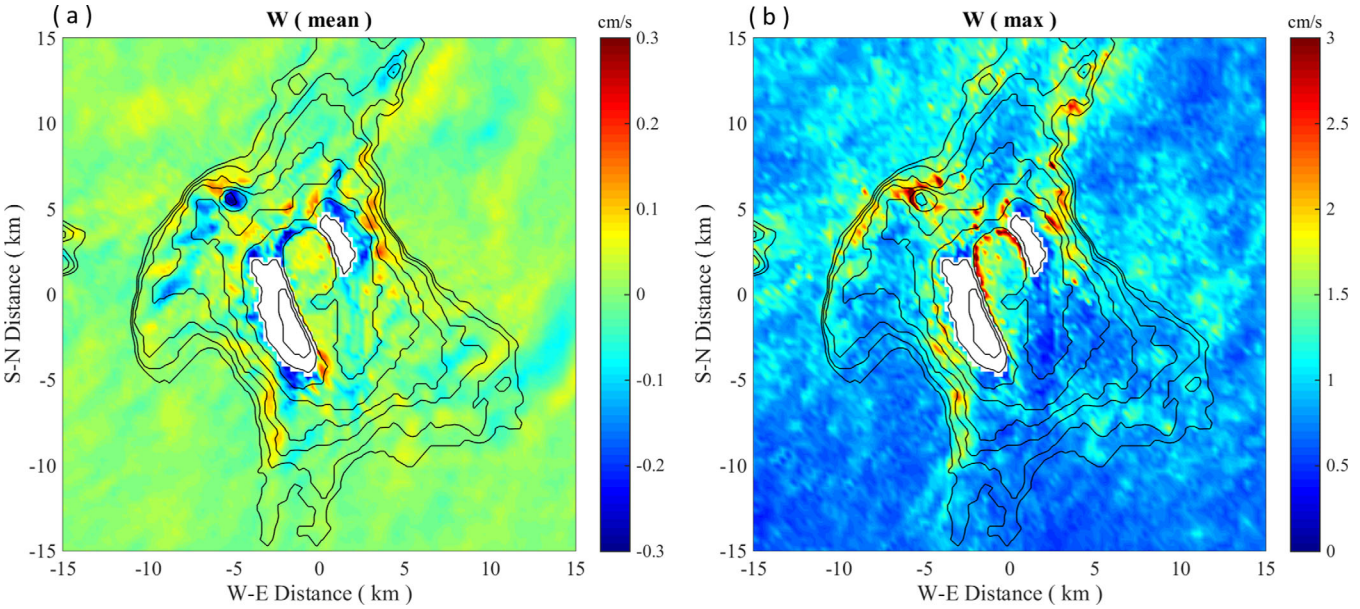

Figure 8. Mean (a) and maximum (b) vertical flows near Axial at 1500 m depth. Black contour lines mark seafloor depth from 1400 to 1800 m in 50 m intervals.

level closest to the crest of the western caldera wall) depths. Time-averaged (29.5 d) vertical flow through the top surface of each of those layers is color-contoured in Figure 9. Superimposed are 29.5 d mean, layer-averaged flow vectors. The sampling regions took their irregular shape from the shape of the caldera at each level except at the open southern end of the caldera (Figure 9).

The lowest layer is of variable depth. At the northern end of the caldera, a bowl-shaped topographic depression makes that region of Layer-1 approximately 40 m deeper at its deepest point than the 10–15 m thickness of Layer-1 nearer the caldera's southern open end. Within Layer-1, much of the flow in the mean recirculates within the caldera. The net vertical flux (positive upward) through the upper lid of this layer is -139 m^3/s (Figure 9a). Along with a small southward inflow at the north end of the caldera, this downward vertical flux into Layer-1 from above results in relatively weak mean outflow at the southern end of the caldera.

The lid of Layer-2 is at 1482 m is the approximate depth of the crest of the caldera wall to the east. Time-mean horizontal in-flow to Layer-2 is strongest along the north-west edge of Axial's caldera where the height of the western caldera wall falls beneath lid-depth. Weaker vertically averaged inflow occurs over the deeper caldera wall at Axial's SE quarter.

Time-averaged upward flow through the upper lid of Layer 2 is about 22 times (3111 m^3/s) the downward flow through the bottom surface of Layer 2. Strongest time-averaged upward flux through Layer-2's lid occurs in the caldera's northeast and southwest, where the strongest lateral out-flux from Layer 2 occurs. Downward flux occurs where horizontal flow is moving away from the caldera wall in the west and into the caldera from the southeastern opening. Still the strongest out-flux from Layer-2 occurs through its top-lid. The sum of fluxes through all bounding surfaces results in time-mean circulation throughout most of the caldera region in Layer-2 that is to the south.

The vector pattern of Layer-3 time-averaged horizontal flow is similar to that at the 1482 m level but flow is stronger. Net upward flux at the top of the layer is 4483 m^3/s, only 44% greater than the value of the flux entering Layer-3 via its bottom surface. Pronounced up-flow occurred where the horizontal flow meets the tallest part of the western wall. The relatively strong outflow at the southern end of the caldera in Layer 3 is $\sim$50 to $\sim$120 m above the depth of the local caldera floor, a height interval in which some hot-vent neutrally buoyant hydrothermal plumes at Axial are likely to be found. They consequently would be most influenced by the flow patterns of Figure 9c. It is also clear from all three plots that mean flow is preferentially inward at the northern end and outward at the southern end of Axial's caldera. Together with the pattern of mean flow outside the caldera (Figure 6), these patterns leave little doubt that some of the fluid and its

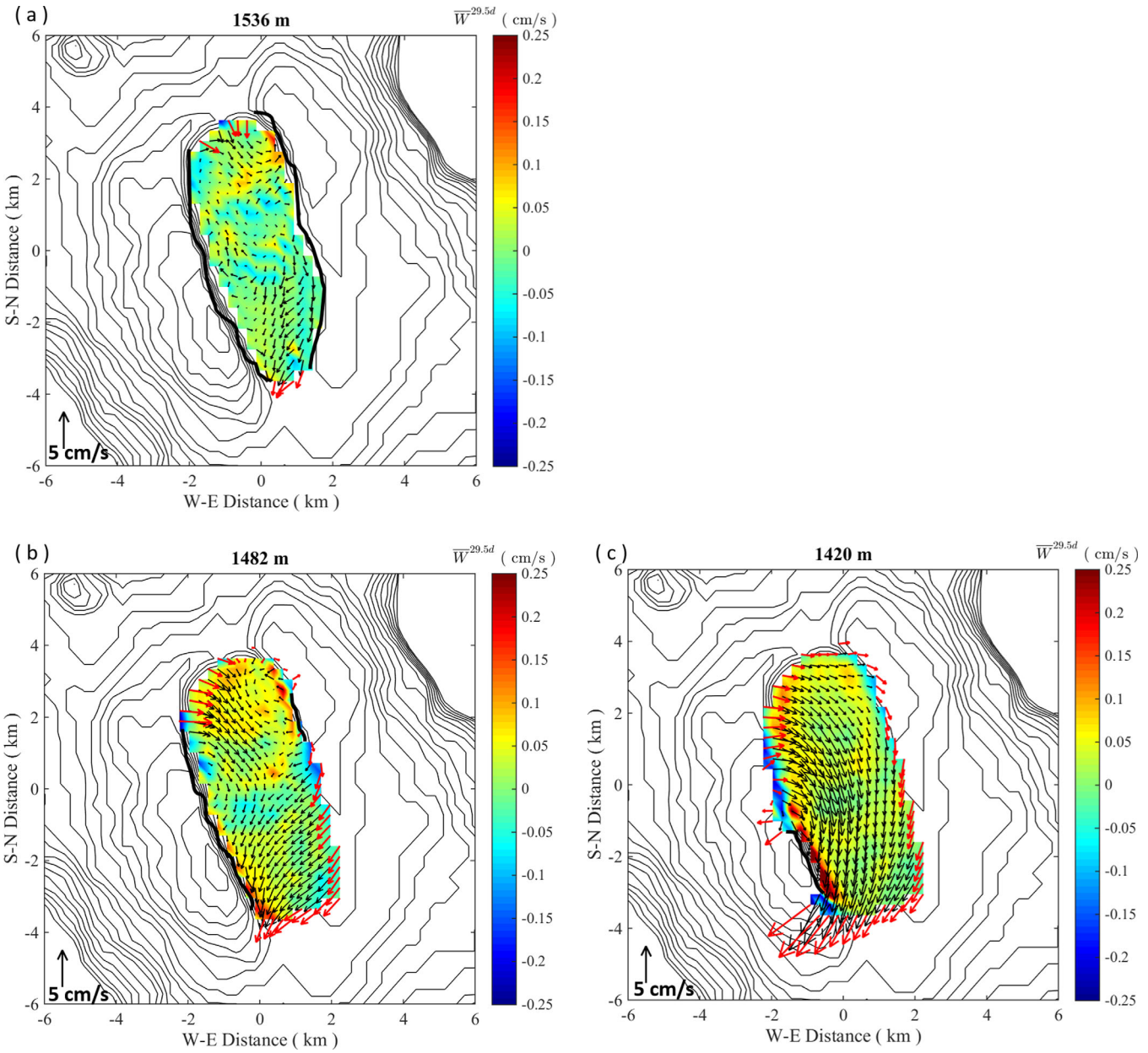

Figure 9. Contours of 29.5 day average vertical flow through three horizontal planes. Arrows represent horizontal flows temporally (29.5 d) and vertically averaged over layers defined by the seafloor and these planes (a) from seafloor to 1536 m, (b) 1482 to 1536 m, and (c) 1420 to 1482 m. Black arrows represent flow in the interior. Red arrows represent flow averaged over layer depth passing over a deeper caldera wall. Heavy black lines in each plot indicate caldera walls impenetrable to horizontal flow.

material content that advect out of the caldera at its southern end will be recirculated into the caldera via flow crossing above less prominent caldera walls at Axial's northern end.

3.3. Oscillatory Flows

3.3.1. Topographic Amplification

E-W cross sections over the top of Axial at $y = 0$ of the amplitudes of (a) the diurnal ($K_{1)}$ and (b) semidiurnal (M_2) oscillations reveal the extent of topographic trapping at the K_1 subinertial frequency and the contribution of internal waves at the M_2 suprainertial frequency (Figures 10a and 10b). Those amplitudes (and those of Figures 10c and 10d) were isolated from model current time series in each computational cell via Fourier analysis. Using the clockwise and anticlockwise complex-number Fourier components at the relevant frequency the major axes of the K_1 and M_2 tidal ellipses within each cell were calculated and color-contoured.

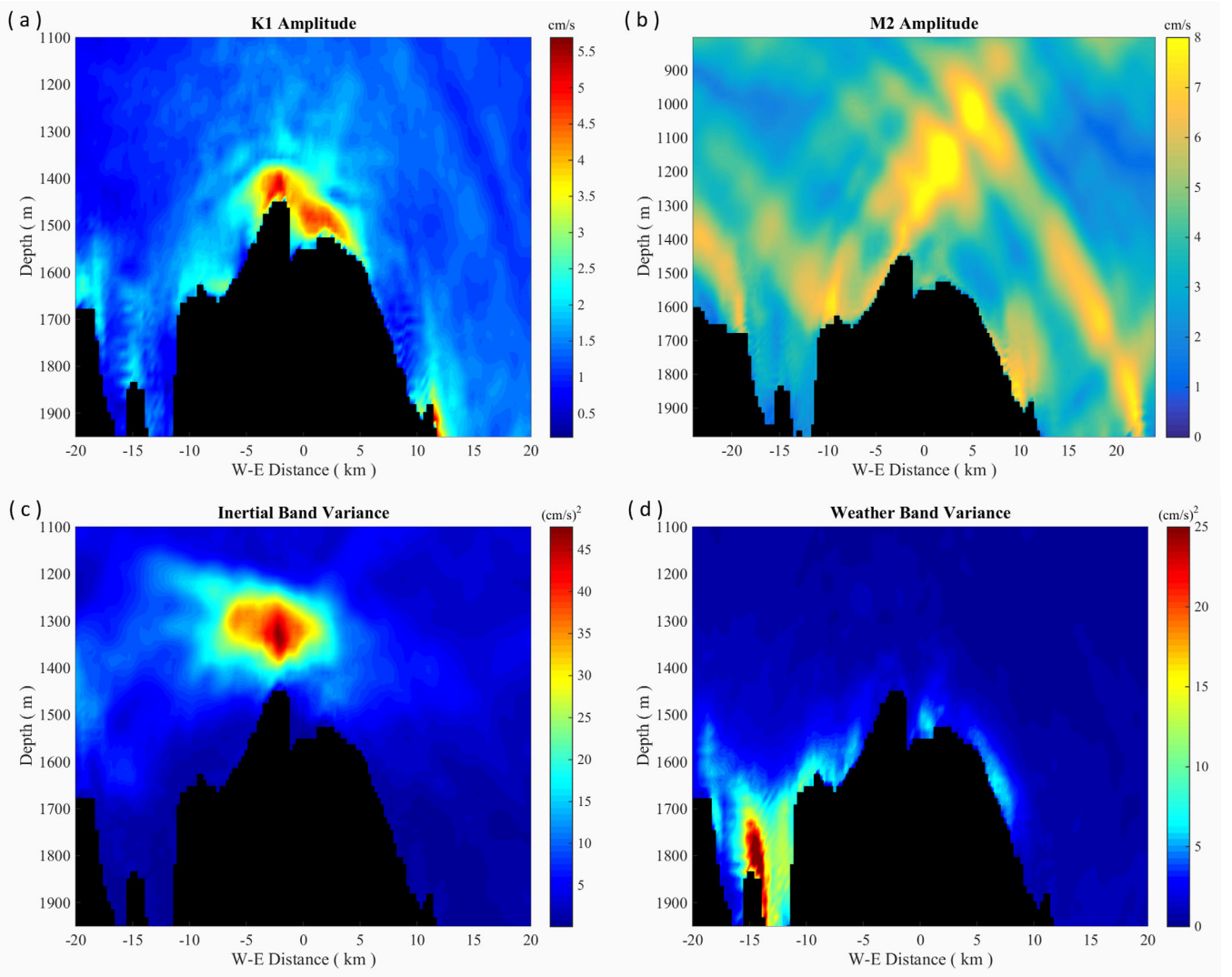

Figure 10. Amplitudes over Axial on the plane $y = 0$ of the (a) diurnal (K_1) and (b) semidiurnal (M_2) tidal constituents and energy variances in (c) inertial and (d) weather bands. The vertical/horizontal scales and color bar for the M_2 differ from the others to better illustrate its wave-train patterns.

Modeled K_1 currents are seen to be amplified over the summit region (Figure 10a). This spatial pattern is consistent with previous observations [*Lavelle, et al.*, 2003]. The maximum amplitude of K_1 currents reaches $>$5 cm/s, which is close to the measurement ($\sim$7 cm/s) at the mooring north of the caldera and 1550 m depth (Figure 1b). Interestingly, the amplification is much weaker just above the seafloor within the caldera. The pattern of M_2 amplitudes is much different (Figure 10b). At the suprainertial frequency, wave trains of M_2 internal tidal currents that originate from the summit of Axial and adjacent topography high points propagate into the distal ocean. Amplifications of the M_2 baroclinic currents are as much as four times the barotropic M_2 amplitude at locations both above and below summit depth. The time and space density of current meter observations over Axial is presently insufficient to confirm this model result.

In addition to these specific tidal constituents, variances of modeled currents over (c) the near inertial band (1.4–1.6 cycle/d) and over (d) the weather band (WB, 3-–6 day period) were also calculated. In these cases, the complex amplitudes of both clockwise and anticlockwise Fourier components were squared and summed over all frequencies in the corresponding frequency bands to represent those variances. Results show inertial band currents are amplified directly over and within $\sim$200 m above the seamount's summit while nearly absent below summit depth (Figure 10c). Atmospheric forcing, such as wind stress, can generate large inertial oscillations in the surface ocean. Part of the surface-generated inertial energy exits the

mixed layer as internal waves that propagate downward to the deep ocean [*D'Asaro et al*., 1995; *Thomson et al*., 1990]. During their downward propagation, the frequencies of those near-inertial waves are usually blue-shifted to suprainertial band [*Kundu and Thomson*, 1985]. This is reflected in the deep currents measured at Axial. At 950 m depth, the peak of the inertial energy is at 1.47 cycle/d (Figure 4a), which is slightly larger than the local inertial frequency: 1.44 cycle/d considering a spectral resolution of 0.02 cycle/d corresponding to the 45 day duration of the current measurements. The field observations reported by *Lavelle et al*. [2003] shows there is higher inertial-band energy at 1300–1400 m than deeper levels, a result consistent with the distribution reported in Figure 10c.

Within the weather band, the most intense amplification occurs in the saddle region connecting Axial and Brown Bear, while weaker amplification occurs over the flanks of Axial (Figure 10d). This spatial distribution of WB energy is consistent with the previous, but sparse field observations of *Cannon and Pashinski* [1990] and *Lavelle et al*. [2003].

In the case of subinertial frequencies such as the K_1 and weather band, amplified baroclinic motions can be excited near a seamount as topographically trapped waves. For example, diurnal tidal currents that are broader than the seamount can excite azimuthal mode-one waves that propagate around the seamount in clockwise direction [*Chapman*, 1989; *Brink*, 1989; *Codiga and Eriksen*, 1997]. Conceptual models used to describe those amplified baroclinic motions include near-resonant seamount-trapped topographic waves [*Brink*, 1989], forced damped seamount-trapped topographical waves [*Brink*, 1990; *Codiga*, 1997], and vortex-trapped internal waves [*Kunze et al*., 1995; *Kunze and Boss*, 1998; *Kunze and Toole*, 1997]. Using the linear baroclinic model of *Brink* [1990], *Lavelle et al*. [2003] investigated the causal mechanism for the amplified diurnal and WB motions at Axial. Their results suggested both diurnal and WB currents share characteristics of forced damped topographical waves.

3.3.2. Baroclinic Velocities

A snapshot of E-W baroclinic velocity, i.e., $u_{bc} = u - \langle u \rangle_z$, where u and $\langle u \rangle_z$ are the full E-W velocity and its vertical average (Figure 11) represents the full-frequency spectrum composite of baroclinic motions. Internal waves are seen to propagate upward and outward from Axial and from a smaller topographic feature ~20 km to the east. These internal waves are a consequence of barotrophic currents, primarily M_2 tidal (Figure 10b), interacting with rough topography. A snapshot taken 6 h later shows similar pattern with near 180° phase change. The generation of internal waves leads to strong vertical shear above the summit of Axial, which enhances mixing of the water column in that region. Furthermore, according to *Chen and Beardsley* [1995], the generation of internal tides contributes to the formation of the residual clockwise circulation around elevated topography like Axial through nonlinear interactions between barotropic and internal tidal currents as well as between internal tidal currents themselves.

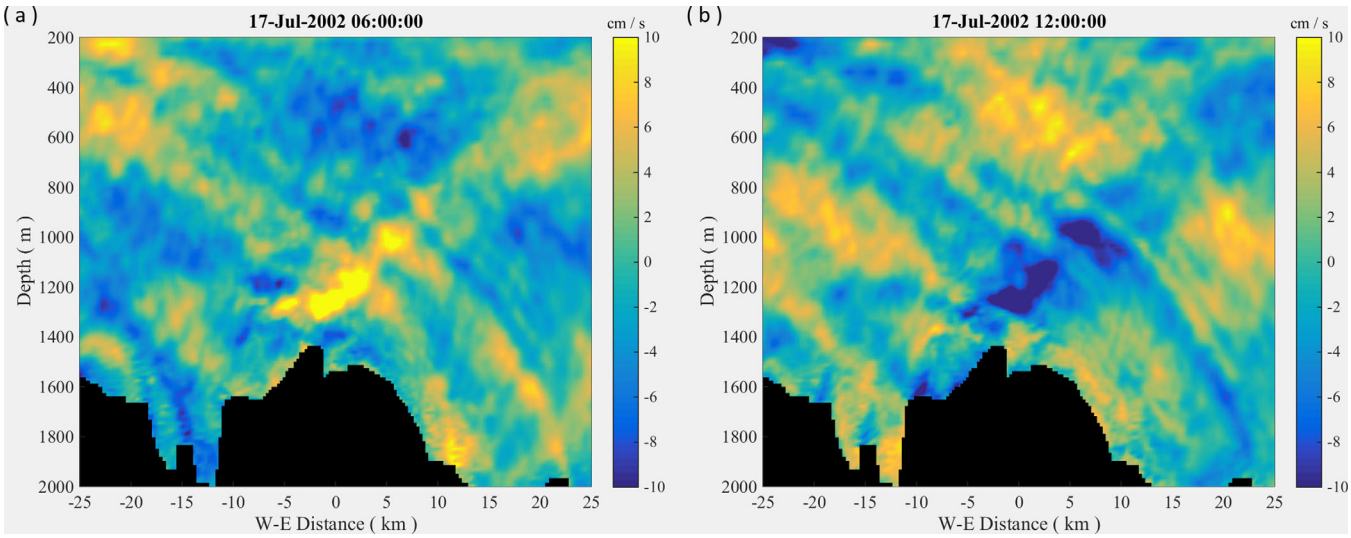

Figure 11. (a) Snapshot of model E-W baroclinic velocity (u_{bc}) across the top of Axial (y = 0) on 17 July 2002 at 06:00 UTC, 27 days into the simulation, (b) same as (a) but 6 h later. Note the near 180° phase change between the wave-train features in the two snapshots.

3.4. Hydrography

3.4.1. Time-Mean Distributions

The hydrography above Axial bears the effects of the spatially and temporally varying currents there. Those effects show up easily both in the 29.5 day means of potential temperature ($\Delta\theta$) and salinity (ΔS) anomalies (Figures 12a and 12b, where $\Delta\theta$ and ΔS are differences, respectively, of θ and S from background values) and in the vertical displacement of isopycnals (ΔZ), where ΔZ is the difference between the depth of an isopyncal over the seamount and in the background region (Figure 12c). The most prominent features in the $\Delta\theta$ and ΔS transects are the domes of cold and briny water above Axial's summit. Cores of both domes (e.g., $\Delta\theta < -0.05$°C) extend laterally nearly 10 km and vertically ~100 m above the highest point of the summit. Below summit depth, colder and saltier water drape over the flanks. The associated consequence is that isotherms and isohalines bow upward above and plunge downward into the seamount's flanks below the summit (Figures 12a and 12b). The potential density anomaly ΔZ displacement is as much as 80 m within the core of the dome (Figure 12c).

Within the caldera itself these long-term-averaged isopleths are seen to be far from horizontal as intuition might otherwise suggest. For example, the 2.35°C isotherm bows upward over the eastern caldera wall and then plunges downward to the base of the western caldera wall (Figure 12a). Despite these substantial horizontal gradients, because these anomalies are the result of local currents and mixing shaped by the local topography, and because these results do not include effects of hydrothermal discharge, plots of potential temperature versus potential density, or salinity versus potential density will remain unchanged in the presence of the cold and briny water. These lateral gradients in the caldera would otherwise have consequences for the extraction of anomalies of temperature attributable to hydrothermal heating [e.g., *Baker and Hammond*, 1992].

Similar hydrographic features, so called "cold domes," have been observed above seamounts and ridges in numerous previous studies [*Owen and Hogg*, 1980; *Roden*, 1987, 1991; *Comeau et al*., 1995; *Lavelle*, 2006, 2012]. *Lavelle* [2012] attributes the formation of a "cold dome" over an idealized model ridge to gradients in eddy heat flux, i.e., gradients in the time-averaged correlations of oscillating currents and temperature. These gradients can be alternately viewed as source/sink terms in the equation of the time-averaged transport of heat. The eddy flux gradients were found to be largest and negative directly over the ridge, serving as a sink to lower temperatures there.

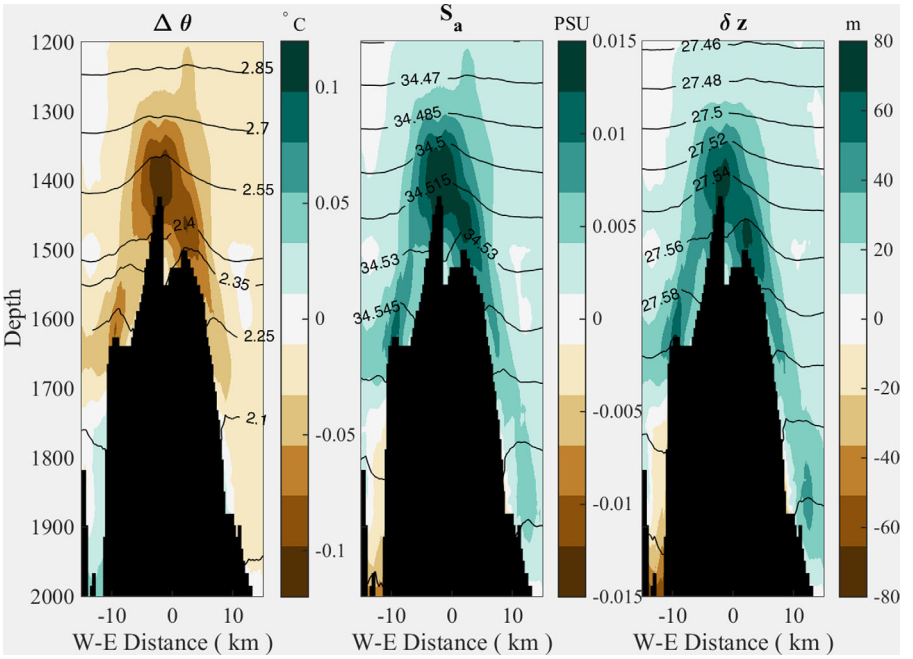

Figure 12. Contours across Axial on the E-W plane $y = 0$ of 29.5 day averaged distributions of (a) potential temperature anomaly ($\Delta\theta$); (b), salinity anomaly (ΔS); and (c) vertical displacement of isopycnals (ΔZ). Line contours in Figures 12a–12c denote potential temperature, salinity, and the density anomaly (i.e., $\varrho - 1000$) kg/m^3, respectively.

3.5. Tracer Dispersal Experiments

The dispersion of material, e.g., dissolved chemicals, fine-size hydrothermal minerals, larvae of vent fauna, or microbes flushed from underground, originating in Axial's caldera is of considerable interest as previously cited. In this study the tracer is neutrally buoyant and dynamically inactive. Cases where gravitational settling, animal motility, or large tracer concentrations affecting density values that would play a role in dispersion are left for future study.

In the first experiment, a tracer was released from a source inside the caldera near its southwestern end at the location which is called ASHES vent field (green square, Figure 14). ASHES is one of the major study sites of OOI's Cabled Array, a site where a high definition camera [*Delaney et al*., 2016] and other instruments connected to the observatory are being used to monitor vent macrofaunal communities and their interactions with oceanic and hydrothermal fluid flow. The model source was made to span four grid cells with a total area of 3×10^5 m^2 horizontally and was made to be 50 m vertically starting at the seafloor. The tracer was released continuously for a period of 30 days, beginning just after the initial 10 day fluid spin-up interval. This experiment begins the study of dispersal patterns of vent-generated materials (e.g., larvae from vent-hosted fauna, hydrothermal chemical species from sources) originating at ASHES.

The resulting tracer plume is depicted in three time snapshots (1, 6, and 15 days) in Figure 13 as logarithmic normalized tracer concentrations ($\log_{10}C$) vertically averaged over 1300–1600 m depths at 1, 6, and 15 days following the start of tracer release. Vertical profiles of horizontally integrated tracer concentrations (not shown) sampled at the same times shows the maximum concentrations remain in the 1500–1550 m depth interval, but the concentrations disperse vertically reaching ~200 m above the crest of the western caldera wall by 15 days. This vertical spreading is a consequence not only of vertical turbulent diffusion but also stirring by the complex character of vertical fluid movement (e.g., Figures 8 and 9) up, down, and over the caldera walls and other irregular topographic features.

The experiment shows the tracer leaves the ASHES vent field area of the caldera at its open southern end (Figure 13a) as would be expected based of the flow patterns of Figure 9. Once outside the caldera, the tracer is swept by the clockwise circulation (Figure 6) toward the northwest along the western flank. Some of the tracer must then reenter the caldera within flow that tops the lower caldera walls to the north, while the remaining fraction continues around the outside of the caldera in the anticyclonic toroidal flow. The net result is tracer that both refills the caldera and circles the caldera in the clockwise direction. By day 6 (Figure 13b), the whole caldera is filled with recirculated tracer from the north and the tracer from the source in an episodic northward flow that occurs on day 4 and 5 (see Movie S1 in supporting information). At day 15 (Figure 13c), the entirety of the caldera contains tracer close to the largest concentration anywhere in the entire tracer field even though the source is localized at the southern end and mean flow is outward from the caldera at the source site.

Over the same 15 day time period (Figure 13c) a small fraction of the tracer has increasingly dispersed outward away from Axial to the southwest following the contours of the saddle topography connecting Axial and Brown Bear. The southwestward plume limb is reminiscent of the observed distribution of material surrounding Axial that contributed to the vertically integrated optical backscatter intensity anomaly during August 1998 [*Lavelle et al*., 2003]. Those same observations show the halo of scatterers surrounding Axial in the same fashion as is represented in Figure 13c. The anticyclonic toroidal flow dominates the dispersion of material leaving the caldera. While it may be serendipitous that regional flow at the time of observations and during the month of model simulation were both to the southwest, some CTD-based evidence exists to suggest that long-term averaged flows off the Juan de Fuca Ridge are to the west [*Cannon and Pashinski*, 1993].

A second tracer experiment was conducted to look at the residence time of a passive tracer released near the seafloor at the northern end of the caldera close to the vent field CASM. Knowing the residence time within the caldera is important for studying the dispersal and retention of larvae spawned from local vent fields and the deposit of hydrothermal chemicals/minerals. In this experiment, the source was a parallelpiped that spanned four grid cells with a total area of 3×10^5 m^2 horizontally (black box in Figure 14a) and the 50 m vertically immediately above the seafloor. In this case, tracer was released over a period of 2 days.

The experiment shows tracer quickly fills the caldera in prevailing southward flow and exits the caldera from its southern opening as would be expected based of the flow patterns in Figure 9. In the meantime, a

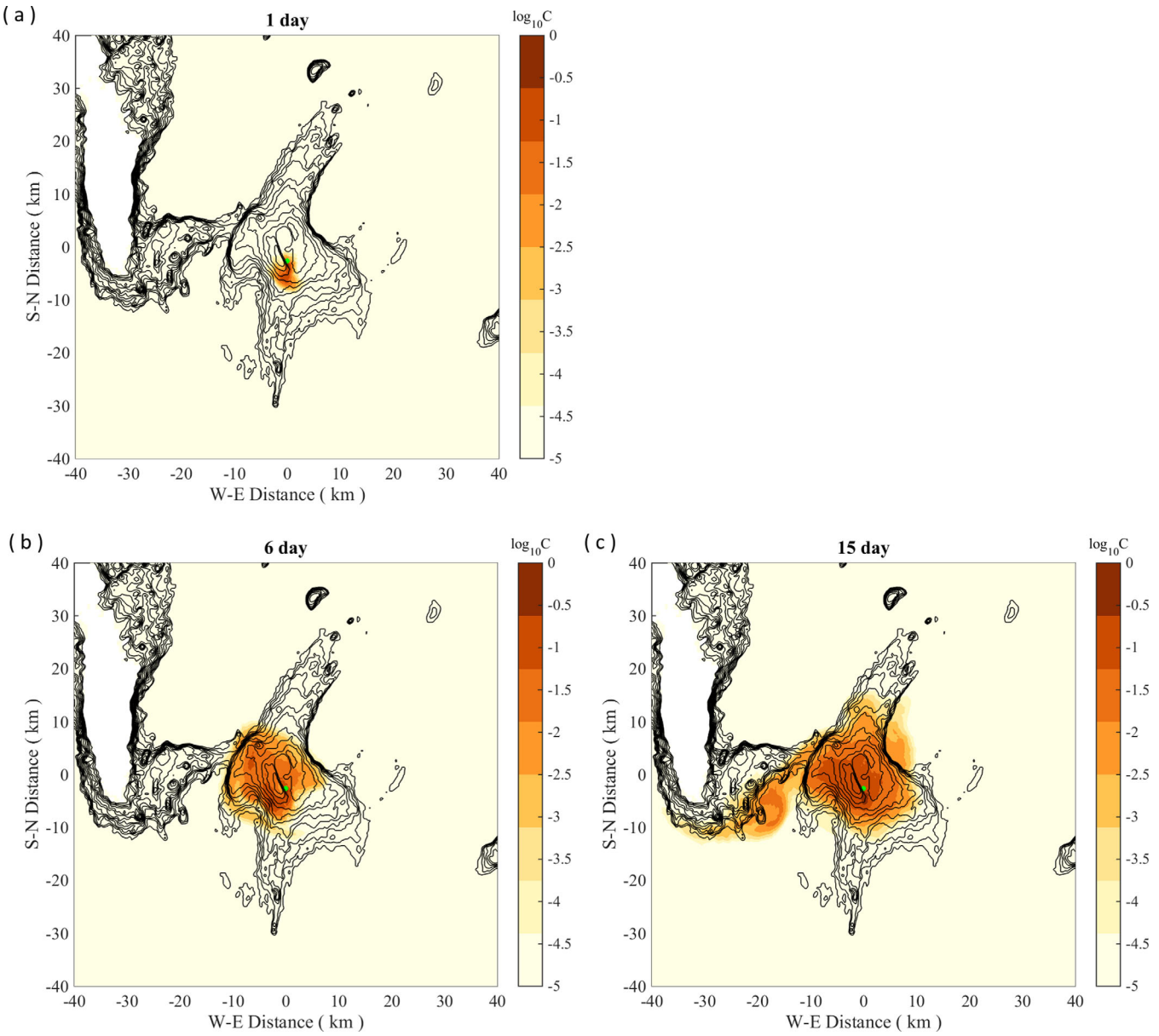

Figure 13. Snapshots of the vertically averaged (1300–1600 m) tracer concentrations on a logarithmic scale at (a) 1, (b) 6, and (c) 15 days after the beginning of tracer release. Concentrations are relative. The green square marks source location.

fraction of tracer leaves the caldera through the saddle at the northern end of the caldera, which is then swept by the clockwise circulation (Figure 6) toward southeast along the eastern flank. Those two streams of tracer coalesce at the southern end and circle around the outside of the caldera in clockwise direction (see Movie S2 in supporting information). Following the cessation of the tracer release, the total mass within a control volume defined by the caldera walls and their upward projection to a depth of 1482 m (top of eastern wall) was then computed. Results as a fraction of tracer remaining in the control volume are shown in Figure 14b. Tracer mass decreases to 10% of its starting value in 8–9 days.

This relatively rapid decline in tracer mass injected into a small area of the deep bowl at the caldera's northern end demonstrates that the deep bowl region is not a quiet pool in which microbes, larvae of macrofauna, or any other caldera-sourced materials might linger. Current patterns (Figure 9a) shows that mean upward flow would advect some of that deep-sourced tracer to a height where eastward flows at the NE end of the caldera would advect it eastward and out of the caldera or, more likely, either southward at

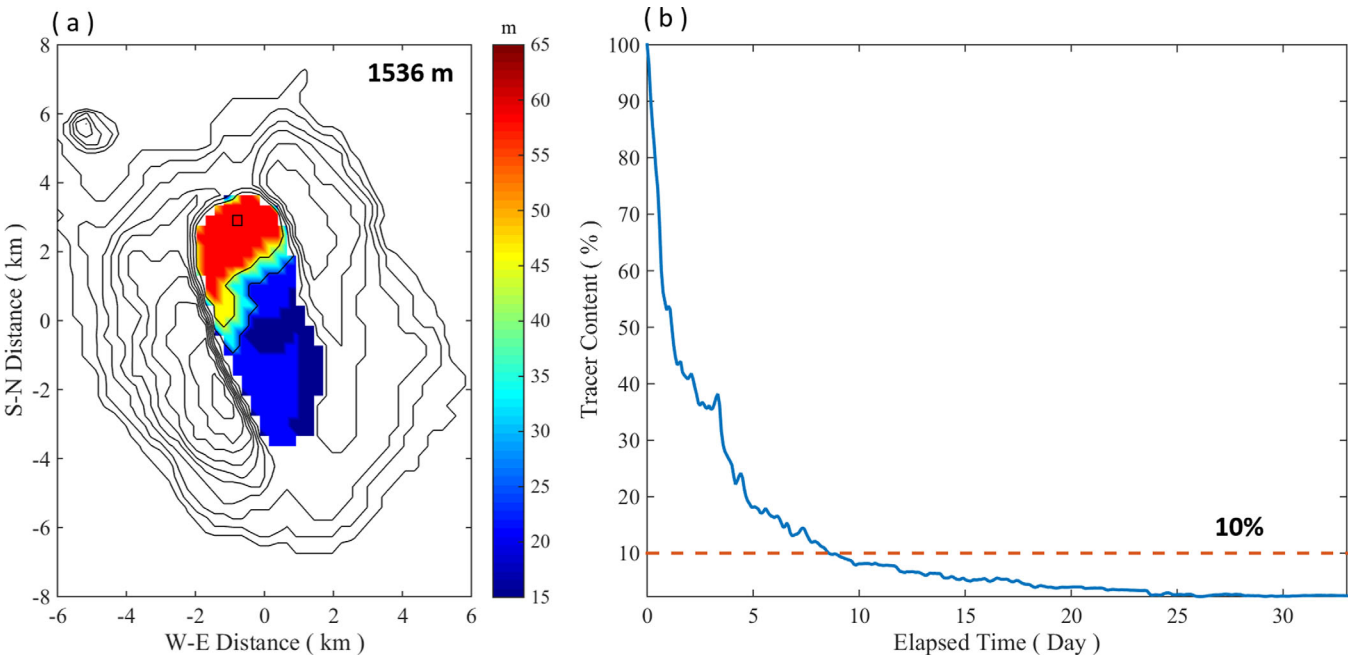

Figure 14. (a) Depth detail within the caldera proper, with depth referenced to a horizontal plane at $z = 1536$ m. The black box marks the location of tracer source. (b) Tracer mass as a function of time within a control volume defined by the caldera walls and their upward projection to a depth of 1482 m (top of eastern wall) during the second tracer release experiment. Elapsed time begins after the cessation of tracer release on 3 July 2002 00:00. The dotted line marks the fraction used to define flushing time.

intermediate depth (1536–1482 m) out the south end of the caldera or upward to a layer of even much stronger southward flow, both of which would ultimately cause it to be entrained into the toroidal flow circulating the summit (Figure 6).

4. Concluding Remarks

4.1. Model Limitations

Because Axial Seamount is a well-known site of both on-going hydrothermal discharge as well as occasional magmatic events that extrude lava onto the seafloor, a natural question to ask is how those chronic or ephemeral heat sources affect circulation and transport as presented in this paper. The answer lies beneath the challenging task of adding either of those heat sources to the model in a plausible way. In the case of hydrothermal discharge, the limitation is one primarily of scale matching. In the case of the lava flows, it is more an issue of not knowing a suitable temporal-spatial description of heat flux from newly placed, crusting, and cracking rock.

At the core of the scale mismatch for chronic hydrothermal discharge is the fact that the scale of vent fields at Axial is on the order of 10 m, 30 times smaller than the smallest grid cell in this model, which as a regional model reaches ~50 km N, S, E, and W beyond Axial. If the effects of vent field heating were to be properly modeled, grid resolution would need to be, at a maximum, 5 m and, importantly, the model description would have to be nonhydrostatic based on the criterion of *Marshall et al.* [1997] described earlier. A nested grid model with nonhydrostatic dynamics at a 5 m scale resolution for the interior grid(s) matched to the regional hydrostatic-model dynamics at 300 m scale resolution, for example, would be one way to begin to embed venting into a regional model like this one. That approach is beyond our reach presently. A second, more heuristic approach might be to parameterize effects of small scale convection taking place within larger computational cells as is sometimes done for the effects of cumulus cloud convection in regional medium-scale atmospheric models. *Thomson et al.* [2009] used this method to look at mean flow forcing together with parameterized vent field convection on the Endeavour segment of the JdFR using the Princeton Ocean Model. With this type of approach, resulting circulation will depend significantly on the convection parametrization and its underlying assumptions.

4.2. Potential Model Applications

Ocean currents near Axial are the primary dispersion agents of larvae of local vent fauna, smaller microbiological species, and vent chemical effluents The mean anticyclonic toroidal flow around Axial's summit favors, for example, the retention of larvae in the near vicinity of the caldera, which likely increases the likelihood of larvae viability, either by their settling back to natal sites or by colonizing nascent vent fields after eruptions, which may contribute to the relatively high colonization rate of nascent posteruption vent fields at Axial [*Marcus et al*., 2009]. We envision more detailed studies of larval dispersal at Axial by coupling our circulation model to particle tracking algorithms (e.g., modified particle tracking algorithm developed by *Blanton* 1995]) that can account for larval characteristics (e.g., vertical movements) and spawning timing and locations [e.g., *McGillicuddy et al*., 2010].

Beyond studying the dispersion of neutrally or near-neutally buoyant materials, it is feasible to include settling characteristics in addressing particle dispersion at Axial. For example, mid-ocean ridge volcaniclastic deposits and their origin has long been a subject of ongoing debate in the geological research community. A recent study based on sediment samples taken on the summit of Axial found that the deposits have a spatial association to caldera ring-faults and are restricted to the summit area [*Portner et al*., 2015]. Our simulation results exhibit a mean anticyclonic toroidal circulation around the summit of Axial (Figures 6 and 7), which would constrain the dispersal of particles ejected during volcanic eruptions to the summit itself and hence can potentially explain the observed sedimentation pattern. Similar to the first example, a more detailed study on this issue can be done in the future by coupling a particle tracking algorithm with the current model to predict particulate sedimentation pattern based on measured settling velocity [*Barreyre et al*., 2011] and an estimated source profile of the volcaniclastics.

4.3. Consequences of the Flow at Axial

The abrupt topography of Axial and the adjacent areas combine with regional background flows having a wide range of oscillatory components to create spatially complex and temporally variable patterns of circulation and transport around the Axial cabled observatory. Material originating in the caldera, whether biological (e.g., macrofaunal larvae), or hydrothermally sourced chemical species (e.g., Fe, Mn), after initially exiting the caldera, likely remain around or above the summit for several weeks before being dispersed to the distal ocean (see Movie S1 in supporting information).

Circulation within, into, and out of the caldera is complicated, made so by the uneven depth of the caldera walls. Material originating in the caldera can revisit the caldera multiple times before meeting any ultimate fate, including transport into a distal region that would prevent it from returning to the seamount's vicinity. Weaker horizontal flows below 1536 m and generally weak vertical flows through that same level might favor the retention of larvae swimming near the caldera floor.

While hydrothermal plumes have not been explicitly considered in the calculations for reasons already given, those that reach neutral buoyancy at a depth between 1500 and 1400 m, for example, would almost surely be subject to the mean flows of the kind depicted in Figure 9 as well as the oscillatory motion. Results here suggest that the majority of hydrothermal material will leave the caldera at the south end, with some of the same material reentering the caldera in the NW after advecting northward along the outside, western caldera wall. In addition, vertical motion at caldera walls likely lifts some of hydrothermal material above its level of neutrally buoyancy.

Acknowledgments

G. Xu thanks his Woods Hole Oceanographic Institution (WHOI) advisor Chris German for his intellectual support, Houshuo Jiang for sponsoring G. Xu's use of WHOI's cluster computer, and Greg Pike for help with model installation on that cluster. G. Xu was funded by WHOI as a postdoctoral scholar. J. W. Lavelle acknowledges with gratitude the NOAA/Pacific Marine Environmental Laboratory (PMEL) and its Earth-Ocean Interaction Group for emeritus-status support. The bathymetric data used in the model can be downloaded from the Global Multi-Resolution Topography (GMRT) Synthesis of Marine Geoscience Data System (MGDS) (http://www.marine-geo.org/tools/GMRTMapTool). The ocean current time series data used in this work were acquired in 2001–2002 by Glenn Cannon at PMEL. Those data can be accessed in the supporting information.

References

Allen, S. E., and R. E. Thomson (1993), Bottom-trapped subinertial motions over midocean ridges in a stratified rotating fluid, *J. Phys. Oceanogr.*, *23*, 566–581, doi:10.1175/1520-0485(1993)023<0566:BTSMOM>2.0.CO;2.

Baker, E. T., and S. R. Hammond (1992), Hydrothermal venting and the apparent magmatic budget of the Juan de Fuca Ridge, *J. Geophys. Res.*, *97*, 3443–3456, doi:10.1029/91JB02671.

Barreyre, T., S. A. Soule, and R. A. Sohn (2011), Dispersal of volcaniclasts during deep-sea eruptions: Settling velocities and entrainment in buoyant seawater plumes, *J. Volcanol. Geotherm. Res.*, *205*, 84–93, doi:10.1016/j.jvolgeores.2011.05.006.

Berdeal, I. G., S. L. Hautala, L. N. Thomas, and H. P. Johnson (2006), Vertical structure of time-dependent currents in a mid-ocean ridge axial valley, *Deep Sea Res., Part I*, *53*, 367–386, doi:10.1016/j.dsr.2005.10.004.

Blanton, B. (1995), *DROG3D: User's Manual for Three-Dimensional Drogue Tracking on a Finite Element Grid With Linear Finite Elements*, Program in Mar. Sci., Univ. of North Carolina, Chapel Hill, N. C. [Available at http://www.opnml.unc.edu/Particle_Tracking/part_track.html.]

Brink, K. H. (1989), The effect of stratification on seamount-trapped waves, *Deep Sea Res., Part A*, *36*, 825–844.

Brink, K. H. (1990), On the generation of seamount-trapped waves, *Deep Sea Res., Part A*, *37*, 1569–1582.

Cannon, G. A., and D. J. Pashinski (1990), Circulation near Axial Seamount, *J. Geophys. Res.*, *95*, 12,823–12,828, doi:10.1029/JB095iB08p12823.

Cannon, G. A., and R. E. Thomson (1996), Characteristics of 4-day oscillations trapped by the Juan de Fuca Ridge, *Geophys. Res. Lett.*, *23*, 1613–1616.
Cannon, G. A., and D. J. Pashinski (1997), Variations in mean currents affecting hydrothermal plumes on the Juan de Fuca Ridge, *J. Geophys. Res.*, *102*, 24,965–24,976, doi:10.1029/97JC01910.
Cannon, G. A., D. J. Pashinski, and M. R. Lemon (1993), Hydrothermal effects west of the Juan de Fuca Ridge, *Deep Sea Res., Part I*, *40*, 1447–1457, doi:10.1016/0967-0637(93)90122-J.
Cannon, G. A., D. J. Pashinski, and T. J. Stanley (1995), Fate of event hydrothermal plumes on the Juan de Fuca Ridge, *Geophys. Res. Lett.*, *22*, 163–166, doi:10.1029/94GL02280.
Carbotte, S. M., M. R. Nedimović, J. P. Canales, G. M. Kent, A. J. Harding, and M. Marjanović (2008), Variable crustal structure along the Juan de Fuca Ridge: Influence of on-axis hot spots and absolute plate motions, *Geochem. Geophys. Geosyst.*, *9*, Q08001, doi:10.1029/2007GC001922.
Chadwick, W. W., D. A. Butterfield, R. W. Embley, V. Tunnicliffe, J. A. Huber, S. L. Nooner, and D. A. Clague (2010), Spotlight 1: Axial Seamount, *Oceanography*, *23*(1), 38–39, doi:10.5670/oceanog.2010.73.
Chadwick, W. W., Jr., S. L. Nooner, D. A. Butterfield, and M. D. Lilley (2012), Seafloor deformation and forecasts of the April 2011 eruption at Axial Seamount, *Nat. Geosci.*, *5*, 474–477, doi:10.1038/NGEO1464.
Chapman, D. C. (1989), Enhanced subinertial diurnal tides over isolated topographic features, *Deep Sea Res., Part A*, *36*, 815–824.
Chapman, D., and D. B. Haidvogel (1992), Formation of Taylor caps over a tall isolated seamount in a stratified ocean, *Geophys. Astrophys. Fluid Dyn.*, *64*, 31–65.
Chen, C., and R. C. Beardsley (1995), A numerical study of stratified tidal rectification over finite-amplitude banks: Part I: Symmetric banks, *J. Phys. Oceanogr.*, *25*, 2090–2110, doi:10.1175/1520-0485(1995)025<2090:ANSOST>2.0.CO;2.
Codiga, D. L. (1997), Physics and observational signatures of free, forced and frictional stratified seamount-trapped waves, *J. Geophys. Res.*, *102*, 23,009–23,024.
Codiga, D. L., and C. C. Eriksen (1997), Observations of low-frequency circulation and amplified sub inertial tidal currents at Cobb seamount, *J. Geophys. Res.*, *102*, 22,993–23,007.
Comeau, L. A., A. F. Vézina, M. Bourgeois, and S. K. Juniper (1995), Relationship between phytoplankton production and the physical structure of the water column near Cobb Seamount, northeast Pacific, *Deep Sea Res., Part I*, *42*, 993–1005, doi:10.1016/0967-0637(95)00050-G.
Cowles, T., J. Delaney, J. Orcutt, and R. Weller (2010), The Ocean Observatories Initiative: Sustained ocean observing across a range of spatial scales, *Mar. Technol. Soc. J.*, *44*, 54–64.
D'Asaro, E. A., C. C. Eriksen, M. D. Levine, C. A. Paulson, P. Niiler, and P. Van Meurs (1995), Upper-ocean inertial currents forced by a strong storm. Part I: Data and comparisons with linear theory, *J. Phys. Oceanogr.*, *25*, 2909–2936.
Delaney, J. (2015), The first ever detection and tracking of a mid-ocean ridge volcanic eruption using the recently completed, NSF funded, submarine fiber optic network in the Juan de Fuca Region, Abstract #OS41B-06 presented at 2015 Fall Meeting, AGU, San Francisco, Calif., 17 Dec.
Delaney, J. R., D. S. Kelley, A. Marburg, M. Stoermer, H. Hadaway, K. Juniper, and F. Knuth (2016), Axial Seamount-wired and restless: A cabled submarine network enables real-time, tracking of a Mid-Ocean Ridge eruption and live video of an active hydrothermal system Juan de Fuca Ridge, NE Pacific, in *OCEANS 2016 MTS/IEEE Monterey*, pp. 1–8, Monterey, Calif.
Dziak, R. P., and C. G. Fox (1999), The January 1998 earthquake swarm at Axial Volcano, Juan de Fuca Ridge: Hydroacoustic evidence of seafloor volcanic activity, *Geophys. Res. Lett.*, *26*, 3429–3432, doi:10.1029/1999GL002332.
Dziak, R. P., S. R. Hammond, and C. G. Fox (2011), A 20-year hydroacoustic time series of seismic and volcanic events in the Northeast Pacific Ocean, *Oceanography*, *24*(3), 280–293, doi:10.5670/oceanog.2011.79.
Embley, R. W., W. W. Chadwick, D. Clague, and D. Stakes (1999), 1998 eruption of Axial Volcano: Multibeam anomalies and sea-floor observations, *Geophys. Res. Lett.*, *26*, 3425–3428, doi:10.1029/1999GL002328.
Feely, R. A., G. J. Massoth, E. T. Baker, G. T. Lebon, and T. L. Geiselman (1992), Tracking the dispersal of hydrothermal plumes from the Juan de Fuca Ridge using suspended matter compositions, *J. Geophys. Res.*, *97*, 3457–3468, doi:10.1029/91JB03062.
Freeland, H. (1994), Ocean circulation at and near Cobb Seamount, *Deep Sea Res., Part I*, *41*, 1715–1732.
Hogg, N. (1973), On the stratified Taylor column, *J. Fluid Mech.*, *58*, 517–537.
Holloway, G. (1987), Systematic forcing of large-scale geophysical flows by eddy topography interaction, *J. Fluid Mech.*, *184*, 463–476.
Huber, J. A., D. A. Butterfield, and J. A. Baross (2006), Diversity and distribution of subseafloor Thermococcales populations in diffuse hydrothermal vents at an active deep-sea volcano in the northeast Pacific Ocean, *J. Geophys. Res.*, *111*, G04016, doi:10.1029/2005JG000097.
Kelley, D. S., J. R. Delaney, and S. K. Juniper (2014), Establishing a new era of submarine volcanic observatories: Cabling Axial Seamount and the Endeavour Segment of the Juan de Fuca Ridge, *Mar. Geol.*, *352*, 426–450.
Kelley, D., J. Delaney, W. Chadwick, B. Philip, and S. Merle (2015), Axial Seamount 2015 Eruption: A 127 m thick, microbially covered lava flow, Abstract OS41B-08 presented at 2015 Fall Meeting, AGU, San Francisco, Calif., 14–18 Dec.
Kelly, N. E., and A. Metaxas (2008), Population structure of two deep-sea hydrothermal vent gastropods from the Juan de Fuca Ridge, NE Pacific, *Mar. Biol.*, *153*, 457–471.
Kundu, P. K., and R. E. Thomson (1985), Inertial oscillations due to a moving front, *J. Phys. Oceanogr.*, *15*, 1076–1084.
Kunze, E., and E. Boss (1998), A model for vortex-trapped internal waves, *J. Phys. Oceanogr.*, *28*, 2104–2115, doi:10.1175/1520-0485(1998)028<2104:AMFVTI>2.0.CO;2.
Kunze, E., R. W. Schmitt, and J. M. Toole (1995), The energy balance in a warm-core ring's near-inertial critical layer, *J. Phys. Oceanogr.*, *25*, 942–957.
Kunze, E., and J. M. Toole (1997), Tidally driven vorticity, diurnal shear, and turbulence atop Fieberling Seamount, *J. Phys. Oceanogr.*, *27*, 2663–2693, doi:10.1175/1520-0485(1997)027<2663:TDVDSA>2.0.CO;2.
Lavelle, J. W. (2006), Flow, hydrography, turbulent mixing, and dissipation at Fieberling Guyot examined with a primitive equation model, *J. Geophys. Res.*, *111*, C07014, doi:10.1029/2005JC003224.
Lavelle, J. W. (2012), On the dynamics of current jets trapped to the flanks of mid-ocean ridges, *J. Geophys. Res.*, *117*, C07002, doi:10.1029/2011JC007627.
Lavelle, J. W., and W. C. Thacker (2008), A pretty good sponge: Dealing with open boundaries in limited-area ocean models, *Ocean Modell.*, *20*, 270–292.
Lavelle, J. W., E. T. Baker, and G. A. Cannon (2003), Ocean currents at Axial Volcano, a northeastern Pacific seamount, *J. Geophys. Res.*, *108*(C2), 3020, doi:10.1029/2002JC001305.
Lavelle, J. W., A. M. Thurnherr, J .R. Ledwell, D. J. McGillicuddy Jr., and L. S. Mullineaux (2010), Deep ocean circulation and transport where the East Pacific Rise at 9–10°N meets the Lamont seamount chain, *J. Geophys. Res.*, *115*, C12073, doi:10.1029/2010JC006426.

Limen, H., C. Levesque, S. K. Juniper, and S. Kim (2007), POM in macro-/meiofaunal food webs associated with three flow regimes at deep-sea hydrothermal vents on Axial Volcano, Juan de Fuca Ridge, *Mar. Biol.*, *153*(2), 129–139.

Lupton, J., E. Baker, R. Embley, R. Greene, and L. Evans (1999), Anomalous helium and heat signatures associated with the 1998 Axial Volcano event, Juan De Fuca Ridge, *Geophys. Res. Lett.*, *26*, 3449–3452, doi:10.1029/1999GL002330.

Marcus, J., V. Tunnicliffe, and D. A. Butterfield (2009), Post-eruption succession of macrofaunal communities at diffuse flow hydrothermal vents on Axial Volcano, Juan de Fuca Ridge, Northeast Pacific, *Deep Sea Res., Part II*, *56*(19–20), 1586–1598, doi:10.1016/j.dsr2.2009.05.004.

Marshall, J., C. Hill, C. L. Perelman, and A. Adcroft (1997), Hydrostatic, quasi-hydrostatic, and nonhydrostatic ocean modeling, *J. Geophys. Res.*, *102*, 5733–5752.

McGillicuddy, D. J., Jr., J. W. Lavelle, A. M. Thurnherr, V. K. Kosnyrev, and L. S. Mullineaux (2010), Larval dispersion along an axially symmetric mid-ocean ridge, *Deep Sea Res., Part I*, *57*, 880–892, doi:10.1016/j.dsr.2010.04.003.

Opatkiewicz, A. D., D. A. Butterfield, and J. A. Baross (2009), Individual hydrothermal vents at Axial Seamount harbor distinct subseafloor microbial communities, *FEMS Microbiol. Ecol.*, *70*(3), 413–424.

Owens, W. B., and N. G. Hogg (1980), Oceanic observations of stratified Taylor columns near a bump, *Deep Sea Res., Part A*, *27*, 1029–1045, doi:10.1016/0198-0149(80)90063-1.

Pawlowicz, R., B. Beardsley, and S. Lentz (2002), Classical tidal harmonic analysis including error estimates in MATLAB using T-TIDE, *Comput. Geosci.*, *28*, 929–937.

Pingree, R. D., and L. Maddock (1985), Rotary currents and residual circulation around banks and islands, *Deep Sea Res.*, *32*, 929–947.

Portner, R. A., D. A. Clague, C. Helo, B. M. Dreyer, and J. B. Paduan (2015), Contrasting styles of deep-marine pyroclastic eruptions revealed from Axial Seamount push core records, *Earth Planet. Sci. Lett.*, *423*, 219–231, doi:10.1016/j.epsl.2015.03.043.

Resing, J. A., R. A. Feely, G. J. Massoth, and E. T. Baker (1999), The water-column chemical signature after the 1998 eruption of Axial Volcano, *Geophys. Res. Lett.*, *26*, 3645–3648, doi:10.1029/1999GL002350,

Roden, G. I. (1987), Effect of seamounts and seamount chains on ocean circulation and thermohaline structure, in *Seamounts, Islands, and Atolls*, edited by B. H. Keating et al., AGU, Washington, D. C., doi:10.1029/GM043p0335.

Roden, G. I. (1991), Mesoscale flow and thermohaline structure around Fieberling Seamount, *J. Geophys. Res.*, *96*, 16,653–16,672, doi: 10.1029/91JC01747.

Shanks, T. M. (2010), Seamounts: Deep-ocean laboratories of faunal connectivity, evolution, and endemism, *Oceanography*, *23*(1), 108–133.

Thomson, R. E., S. E. Roth, and J. Dymond (1990), Near-inertial motions over a mid-ocean ridge: Effects of topography and hydrothermal plumes, *J. Geophys. Res.*, *95*, 7261–7278, doi:10.1029/JC095iC05p07261.

Thomson, R. E., M. M. Subbotina, M. Marina, and M. V. Anisimov (2009), Numerical simulation of mean currents and water property anomalies at Endeavour Ridge: Hydrothermal versus topographic forcing, *J. Geophys. Res.*, *114*, C09020, doi:10.1029/2008JC005249.

Tivey, M. K., A. M. Bradley, T. M. Joyce, D. Kadko (2002), Insights into tide-related variability at seafloor hydrothermal vents from time-series temperature measurements, *Earth Planet. Sci. Lett.*, *202*, 693–707.

Zimmerman, J. T. F. (1980), Vorticity transfer by tidal currents over an irregular topography, *J. Mar. Res.*, *38*, 601–630.